High-Throughput Screening of Single Atom Co-Catalysts in ZnIn₂S₄ for Photocatalysis

Md Habibur Rahman^a, Yujie Sun^b and Arun Mannodi-Kanakkithodi^a

Abstract

In recent years, $ZnIn_2S_4$ (ZIS) has garnered attention as a promising photocatalyst due to its attractive properties. However, its performance is hindered by its restricted range of visible light absorption and the rapid recombination of photoinduced holes and electrons. Single-atom co-catalysts (SACs) can improve photocatalytic activity by providing highly active sites for reactions, enhancing charge separation efficiency, and reducing the recombination rate of photo-generated carriers. In this work, we perform high-throughput density functional theory (DFT) computations to search for SACs in ZIS encompassing 3d, 4d, and 5d transition metals as well as lanthanides, considering both substitutional and interstitial sites. For a total of 172 SACs, defect formation energy (DFE) is computed as a function of chemical potential, charge, and Fermi level (E_F), leading to the identification of low energy dopants and their corresponding shallow or deep defect levels. Statistical data analysis shows that DFE is highly correlated with the difference in electron affinity between the host (Zn/In/S) atom and the SAC, followed by the electronegativity and boiling point. Among the 60 lowest energy SACs, Co_{In} , Yb_i , Tc_{Zn} , Au_S , La_i , Eu_i , Au_i , Ta_{In} , Hf_{In} , Zr_{In} , and Ni_{Zn} lead to a lowering of the Gibbs free energy for hydrogen evolution reaction, improving upon previous ZIS results. The computational dataset and insights from this work promise to accelerate the experimental design of novel dopants in ZIS with optimized properties for photocatalysis and environmental remediation.

1 Introduction

The depletion of energy supplies and the discharge of harmful substances into the environment have become critical issues for long-term human survival due to the rapid expansion of the global population and industrialization. Consequently, discovering sustainable and environmentally friendly solutions to these problems is becoming increasingly important. Heterogeneous photocatalytic systems, which make use of semiconducting materials, have become a promising solution in this context $^{1-4}$. The photocatalytic process has the potential to efficiently harness solar energy and produce a range of valuable chemical fuels, such as hydrocarbons through CO2 conversion and H_2 and O_2 via photocatalytic H_2O splitting ^{5,6}. Additionally, by efficiently decomposing dangerous and toxic substances, they provide the potential to reduce environmental contamination ^{7,8}. In particular, these semiconducting materials exhibit appealing photocatalytic activity, strong exciton binding energy, non-toxicity, and exceptional photosensitivity.

Wide bandgap materials like ZnO and TiO_2 have a limitation when it comes to photocatalytic applications since they primarily absorb ultraviolet (UV) light, which limits the effective utilization of the solar spectrum⁹. Compared to ZnO and TiO_2 , ultrathin $ZnIn_2S_4$ (ZIS) shows

a smaller bandgap which enables higher absorption in the solar spectrum, including visible light ^{10,11}. Additionally, the layered structure of ZIS creates a large surface area and a higher number of active sites for catalytic processes, which makes it easier to adsorb and activate reactant species ^{6,10}. Also, it is possible to alter the electronic structure and surface properties of ZIS using doping or alloying techniques because both Zn and In are present in the crystal ^{12,13}. Furthermore, ZIS possesses appealing chemical stability, which is necessary for long-lasting and robust photocatalytic application 14,15. However, the limited visible light absorption and relatively high rate of recombination of photogenerated charge carriers limit the photocatalytic performance of ZIS 16,17. Consequently, to tune the photocatalytic activity of ZIS, several strategies have been proposed including methods like van der Waals (vdW) heterostructure configuration, metal doping, vacancy engineering, metal deposition and so on ^{18,19}.

Defect engineering is a widely utilized approach for altering the optoelectronic properties of semiconductors 18,20 . During semiconductor fabrication, defects are unavoidable and can significantly influence the performance of photocatalysts 21,22 . Different types of defects, including vacancies, anti-sites, substitutions, interstitials, grain boundaries, and surface states, have been shown to greatly affect the optoelectronic characteristics of photocatalysts 18,20 . For instance, creating vacancies has been an effective strategy to increase the visible light absorption by introducing impurity states near the Fermi level ($E_{\rm F}$),

^aSchool of Materials Engineering, Purdue University, West Lafayette, IN 47907, USA; E-mail: amannodi@purdue.edu

^bDepartment of Chemistry, University of Cincinnati, Cincinnati, OH 45221 USA

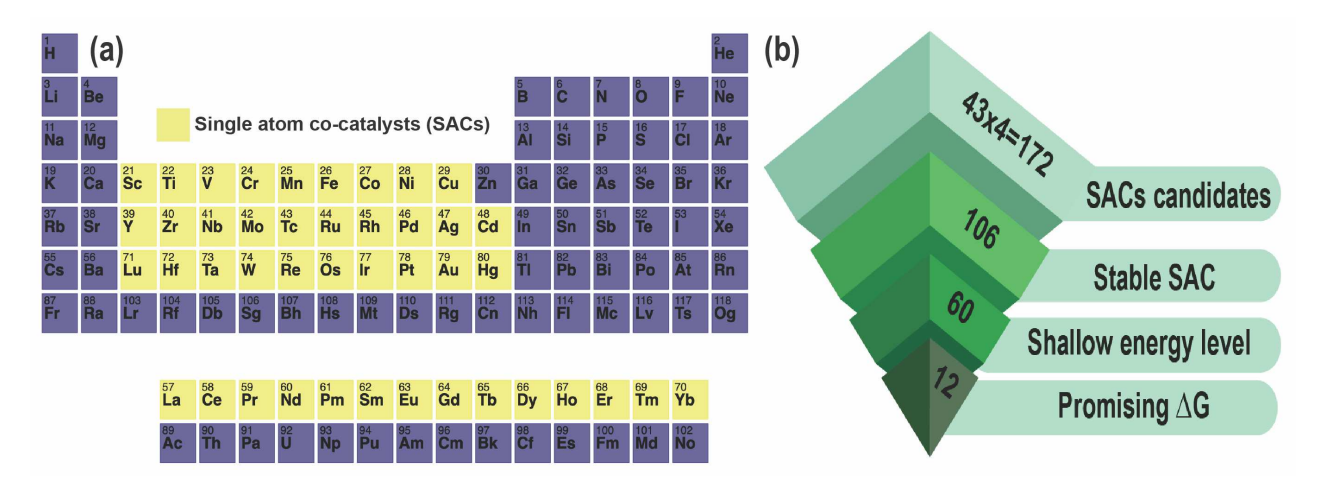


Fig. 1 (a) All single-atom co-catalysts (SACs) analyzed in this study are highlighted in yellow; (b) Screening hierarchy: Out of the 43×4 (total number of sites) = 172 SACs examined, 106 are found to be stable, showing lower energy in comparison to native defects. Among these 106 dominant SACs, 60 demonstrate shallow energy levels, and 12 show improved Gibbs free energy, for photocatalytic Hydrogen Evolution Reaction (HER).

thereby facilitating the transfer of electrons from the valence band (VB) to the conduction band (CB) ^{23,24}. However, these vacancies can also increase the number of electron traps, which can decrease the mobility and stability of photogenerated carriers, ultimately lowering the photocatalytic efficiency ^{25,26}.

Single-atom catalysts (SACs) are atomically scattered metal atoms on a substrate that have become a well-established method for guaranteeing the optimal utilization of catalytically active atoms in heterogeneous catalysis ^{27,28}. Due to their clearly defined and segregated active regions, SACs have distinct benefits over conventional bulk catalysts in terms of selectivity^{29,30}. SACs lead to larger surface area than bulk catalysts, allowing for more effective exposure of active sites to reactants thus promoting better catalytic activity ^{29,31}. Furthermore, SACs can be designed to have customized electronic and optical characteristics, enabling efficient absorption of a wider range of photons, including visible light 30,32. This eventually broadens the range of visible light that can be absorbed and makes it possible to use solar energy more effectively ^{33,34}. The presence of single atoms on a catalyst surface speeds up charge transfer processes, reduces charge carrier recombination, and enhances the separation and migration of photogenerated electrons and holes, all of which are necessary for fostering photocatalytic reactions ^{27,28}. SACs also have the benefit of having tunable catalytic sites which enable precise atomic-level control, improving the catalytic activity for certain reactions ^{29,31}. Due to their distinct active site topologies, SACs also show better selectivity towards target products, allowing for control over reaction pathways and the suppression of undesirable side effects 30,32 .

Additionally, SACs have been used to increase the effectiveness of oxygen evolution reaction (OER) and hydrogen evolution reaction (HER) in the context of H₂O splitting. The electrochemical processes involved in H₂O splitting are made easier by utilizing the active sites in transition metal (TM) SACs, such as Pt, Ni, and Co, which could potentially boost the overall photocatalytic process as well as the production of H_2 gas 13,35 . For example, a study by Shi et al. 36 demonstrated that single Pt atoms on ZIS significantly enhance photocatalytic performance by improving charge separation and minimizing electron-hole pair recombination. Additionally, it could potentially induce a tipping effect that optimizes H adsorption and desorption by promoting efficient proton transfer, which synergistically enhances the thermodynamics and kinetics of the reaction. The reduction of CO2 to CO or other hydrocarbon products has also shown improved catalytic activity in metal-based SACs like Cu and Ag^{27,28}. Additionally, SACs have been used in photocatalytic reactions to degrade organic contaminants. For instance, Pd and Au-based SACs have shown notable effectiveness and selectivity toward the breakdown of colors, insecticides, and medications 30,32. Metal-based SACs, such as those made of Ni, Fe, or Co, hold great promise to enable very effective and long-lasting overall H₂O splitting processes ^{29,31}.

Although the formation of native point defects in ZIS and their impact on photocatalytic activity have been well examined, very little is known about the energetics

of dopants such as TM-based SACs and how they would affect photocatalytic performance ^{37,38}. When dopants are more stable than native point defects within the semiconductor bandgap, they will modify the equilibrium E_F, type of conductivity (p-type, n-type, or intrinsic), as well as the behavior of charge carriers ^{21,22}. To achieve the best optoelectronic performance, it is crucial to accurately estimate the electronic levels that may be introduced by dopants. Deep defect levels can influence charge carrier recombination in multiple ways, unlike shallow donor or acceptor levels located near the band edges ^{20,23}. For instance, deep-level dopants may function as non-radiative recombination centers (i.e., recombination without emitting photons) for minority charge carriers, which can decrease carrier lifetime, hinder carrier collection, and reduce optoelectronic efficiency^{25,26}. Additionally, dopants can either enhance or inhibit the adsorption of organic/inorganic species, thereby influencing the semiconductor's photocatalytic capabilities 18,24. Hence, it is essential to comprehensively assess the stability of dopants in ZIS, their electronic levels, and the resulting equilibrium conductivity. Techniques such as photoluminescence (PL), deep-level transient spectroscopy (DLTS), and cathodoluminescence (CL) can be employed to detect, characterize, and locate impurities in semiconductors ^{22,25}. However, the difficulty in introducing specific impurities or dopants and linking measured levels to particular defects means experimental methods often fall short of providing a complete picture of point defects in semiconductors ^{21,26}. Conversely, density functional theory (DFT) is a powerful tool for simulating point defects and has been widely used to calculate defect formation energies (DFEs) and associated charge transition levels (CTLs) in various crystalline materials 39-44.

In this article, we present a comprehensive highthroughput DFT study of potential SACs for ZIS. Our investigation encompasses the entire 3d, 4d, and 5d TM series, as well as the lanthanide series, totaling 43 candidates. We examine the energetics of these 43 SACs, focusing on four distinct sites: $M_{\rm Zn}$, $M_{\rm In}$, $M_{\rm S}$, and $M_{\rm i}$, where M refers to the specific metal dopant and the subscript is the doping site (Zn, In, S, or interstitial). This approach results in an analysis of $43 \times 4 = 172$ SACs, considering their DFE as a function of $E_{\rm F}$ in 5 different charge states under three different growth conditions, namely S-rich (anion), In-rich (cation), and moderate (between anion and cation rich conditions). These calculations help us identify the relative stabilities of these SACs as well as their shallow/deep nature in the bandgap, following which we simulate their HER-related Gibbs free energies and determine suitable candidates for improved catalytic performance in ZIS. Although our work is mainly concerned with the photocatalytic activity of ZIS, it is important to note that photo-corrosion of ZIS, especially photo-oxidation and metal leaching, is a concern under real-world conditions. SACs may help to prevent photo-oxidation by blocking the active sites on the ZIS surface that can lead to S²⁻ oxidation and degradation of the ZIS ⁴⁵. SACs can also immobilize the Zn²⁺ and In³⁺ ions in the ZIS lattice and prevent metal leaching, which is a common problem under oxidation. This kind of stabilization is very important for the structural reinforcement and durability of ZIS in photocatalytic processes.

2 Methodology

All DFT calculations were performed using a $3 \times 3 \times 1$ monoclinic supercell of ZIS with 126 atoms (18 Zn, 36 In, and 72 S), with lattice constants of a = 20.03 Å, b = 11.60 Å, and c = 25.00 Å. SACs including 3d, 4d, 5d, and lanthanide series elements as pictured in Fig. 1, were introduced in the optimized supercell and geometry optimization was performed considering 5 distinct charge states (q = -2, -1, 0, +1, +2) while keeping the size and shape of the supercell fixed.³⁷ This results in a total of 43 \times 4 (number of defect sites) \times 5 = 860 dopant calculations, in addition to which we simulated a total of 12 native defects, leading to 860 + 12 \times 5 = 920 total DFT calculations. Spin-polarized DFT was performed using the Vienna ab-initio Simulation Package (VASP) and projector augmented wave (PAW) pseudopotentials, with the exchange-correlation energy defined using the Perdew-Burke-Ernzerhof (PBE) functional within the generalized gradient approximations (GGAs)^{39–41}. kinetic energy cutoff of 500 eV was set for the plane-wave basis, and ionic relaxation was performed until the forces on each ion were less than 0.05 eV/Å^{37,46}.

To take into account the impact of on-site Coulomb interactions stemming from the In and Zn atoms, the Hubbard +U correction was applied, with U values of 5 eV and 4.5 eV for In and Zn respectively, following our previous work 46. For GGA+U, the Brillouin zone was sampled using a $1 \times 2 \times 1$ Monkhorst-Pack mesh centered at the Gamma point 37. Furthermore, to prevent interactions between the ZIS surface and its periodic image, a vacuum region of 1 nm was included 37. To achieve accurate predictions of defect levels within the bandgap, the GGA+U relaxed structure is used as input to a single-shot hybrid (mixing the Hartree-Fock and Kohn-Sham theories) HSE06 functional. The DFE (or E^f) and CTL ($\varepsilon(q_1/q_2)$, where a defect transitions from one charge state to another) were calculated using the following equations: 37 :

$$E^{f}\left(D^{q},E_{F}\right)=E\left(D^{q},ZIS\right)-E\left(ZIS\right)+\mu+q\left(E_{F}+E_{VBM}\right)$$

$$+E_{corr}$$
 (1)

$$\varepsilon(q_1/q_2) = \frac{E^f(q_1, E_F = 0) - E^f(q_2, E_F = 0)}{q_2 - q_1}$$
 (2)

Here, E(ZIS) represents the DFT energy of a ZIS supercell without any defects, $E(D^q, ZIS)$ represents the DFT energy of the ZIS supercell containing a defect D in a charge state q, E_{VBM} is the valence band maximum (VBM) of bulk ZIS, μ represents the chemical potential associated with the creation of the defect, and E_{corr} is the charge correction energy which accounts for the interaction between the charged defect and its periodic image, calculated using the scheme developed by Freysoldt et al. 37,47 The Ef is dependent on E_F in such a way that the slope of the E^f versus E_F plot is equal to the charge q^{38} . For each defect in the ZIS compound, the chemical potentials of all atoms are referenced to the lowest energy elemental standard state of each species. The defect CTLs $(\varepsilon(q_1/q_2))$ correspond to specific E_F values where the defect becomes more stable in charge state q_2 than q_1 , independent of μ . In this work, we calculated four different defect levels for each SAC, namely +2/+1, +1/0, 0/-1, -1/-2. The E_F takes a range of values corresponding to the HSE06-computed band gap of 3 eV. The procedure to simulate the HER process on a catalyst surface and calculate the Gibbs free energy is described in Section 3.3 along with a discussion of the associated results.

We note that Freysoldt's image-charge correction method 47 is the most appropriate for our system as it includes the long-range Coulombic and finite-size effects of the defect supercell, which means no additional dipole or quadrupole (Q) corrections are required. In practice, Q cannot be derived directly from the defect charge distribution as the defects could potentially exist in various forms; their wave functions can either be localized or delocalized and they are always accompanied by the screening charges of the host material. To overcome the limitation of periodic boundary conditions and to obtain a rather accurate DFE, we employed a large supercell and applied the Freysoldt correction⁴⁷. This approach aligns with best practices in the field, as demonstrated by other studies 48, which have shown that this correction effectively addresses the issues without the need for further corrections.

3 Results and discussion

3.1 Calculating Chemical Potentials

Prior to computing the energy of SAC doping, we first evaluated the chemical potential limits for ZIS. In thermodynamic equilibrium, the chemical potentials of all native species in ZIS should satisfy the following equations³⁷:

$$\begin{split} \Delta\mu_{Zn} + 2\Delta\mu_{In} + 4\Delta\mu_{S} &= \Delta H(ZIS), \\ \Delta\mu_{Zn} + \Delta\mu_{S} &\leq \Delta H(ZnS), \\ \Delta\mu_{In} + \Delta\mu_{S} &\leq \Delta H(InS), \\ 2\Delta\mu_{In} + 3\Delta\mu_{S} &\leq \Delta H(In_{2}S_{3}), \\ \Delta\mu_{Zn} &\leq 0, \\ \Delta\mu_{In} &\leq 0, \\ \Delta\mu_{S} &\leq 0. \end{split}$$

These conditions are necessary to prevent the decomposition of ZIS into elemental Zn (hexagonal), In (trigonal), and S (monoclinic), or to binary compounds like ZnS (trigonal), InS (orthorhombic) and In_2S_3 (tetragonal). The formation energy of ZIS, denoted as $\Delta H(ZIS)$, is defined as:

$$\Delta H(ZIS) = E(ZIS) - E(Zn) - 2E(In) - 4E(S),$$

and similarly, the formation energies of ZnS, InS and In_2S_3 are defined as:

$$\Delta H(\mathrm{ZnS}) = E(\mathrm{ZnS}) - E(\mathrm{Zn}) - E(\mathrm{S}),$$

$$\Delta H(\mathrm{InS}) = E(\mathrm{ZnS}) - E(\mathrm{In}) - E(\mathrm{S}),$$

$$\Delta H(\mathrm{In}_2 S_3) = E(\mathrm{In}_2 S_3) - 2E(\mathrm{In}) - 3E(\mathrm{S}).$$

Herein, E(system) represents the total DFT energy per formula unit (p.f.u.) of the given system. The chemical potentials of Zn, In, and S are referenced against their respective elemental standard states, such that:

$$\mu_{\mathrm{Zn}} = \Delta \mu_{\mathrm{Zn}} + E(\mathrm{Zn}),$$

$$\mu_{\mathrm{In}} = \Delta \mu_{\mathrm{In}} + E(\mathrm{In}),$$

$$\mu_{\mathrm{S}} = \Delta \mu_{\mathrm{S}} + E(\mathrm{S}).$$

For Zn-rich conditions, the stability of ZIS with respect to the precipitation of excess Zn limits the value of $\mu_{\rm Zn}$, which can be mathematically expressed as $\mu_{\rm Zn}=E({\rm Zn})$ and $\Delta\mu_{\rm Zn}=0$. The same analogy applies to In-rich and

S-rich growth conditions. The stable region of ZIS may be further restricted by eliminating the formation of alternative phases. Additional equations are presented in the supporting information (SI) to define the chemical potential limits corresponding to SAC doping, which involves additional conditions pertaining to the formation of impurity phases such as Sc_2S_3 or TiS. All revelant impurity phases and elemental standard state structures of SAC candidates are the lowest energy structures available in the Materials Project (MP) database ⁴⁹. For HSE06, we performed single-shot calculations on the GGA relaxed reference compounds as obtained from the MP database.

3.2 Defect Formation Energies

We performed high-throughput DFT computations to investigate the charge-dependent energetics of 43 possible SAC candidates at 4 possible defect sites in ZIS. In our analysis, any defect transition level that occurs within 25% to 75% of the bandgap is categorized as deep, and all other levels are classified as shallow. We first computed the DFE as a function of the E_F (where E_F spans from the VBM to the CBM) using only the GGA+U energies. Fig. S1 shows a visualization of the entire dataset of GGA+U-computed native defects and SAC dopants, in terms of the neutral state DFE values at In-rich and S-rich conditions, and in terms of all the transition levels, namely ε (+2/+1), ε (+1/0), ε (0/-1), and ε (-1/-2). Furthermore, to assess the extent of DFT optimization on the defect properties, we plotted a DFT-unoptimized (single-shot energy from pristine defect structure) vs DFT-optimized energy in Fig. **S2**. It can be seen that the extent of geometry optimization (difference in optimized vs unoptimized energy) is minimal for vacancies and most interstitials, but significant for some substitutional defects.

The GGA+U calculations included previously established U values for Zn and In 46 , but we chose not to initialize any U values for the SAC dopants, owing to the difficulty in determining suitable values for each via empirical fitting or self-determination methods, including the linear response theory 50 . To assess the impact of the U parameter on our results, we performed geometry optimization for ZIS with and without a +U correction. This comparative analysis yielded lattice parameters (a=6.70~Å vs 6.71~Å, b=3.87~Å vs 3.88~Å, c=12.48~Å vs 12.50~Å) and bond lengths for Zn-S (2.35~Å vs 2.34~Å) and In-S (4.62~Å vs 4.63~Å) from GGA+U vs GGA, indicating that the geometry inputs for the HSE06 calculations were largely unaffected by the choice of U parameters. This

observation underscores the reliability of our crystalline structures against the variability introduced by U values; rather, it's the Kohn-Sham eigenvalues and the energy levels that are highly dependent on the choice of U.

Fig. 2 shows a complete visualization of the HSE06computed defect properties. We find that the DFEs show a wide range of values from \sim -1 eV to nearly 12 eV with S-rich DFE typically higher than In-rich DFE. While a few (0/-1) and ε (-1/-2) transitions occur within the bandgap (0 to 3 eV), almost every ε (+2/+1) and ε (+1/0) level seems to appear in the bandgap, meaning these transitions may be the primary source of mid-gap levels arising from the SACs. A critical aspect of our findings is illustrated in Fig. 3 in terms of a parity plot between the DFE for all 5 charge states (taken at the VBM, i.e., at $E_F=0$) and defect levels calculated using GGA+U and HSE06. Remarkably, the data reveals a strong correlation with a few notable exceptions, underscoring the reliability of GGA+U in predicting trends that are consistent with the more rigorous HSE06 calculations. This correlation not only validates our computational strategy but also reinforces the utility of GGA+U for preliminary analyses in defect studies.

As an extension to our recent work³⁷, we first computed the HSE06 DFEs of all native point defects in ZIS, namely vacancies (V_{Zn}, V_{In}, V_S), anti-sites (Zn_{In}, Zn_s, In_{Zn}, In_s, S_{Zn}, S_{In}), and self-interstitials (Zn_i, In_i, S_i). Anti-site defects Zn_{In} and In_{Zn} are found to be the lowest energy acceptor and donor defects respectively, pinning the equilibrium E_F slightly to the right of the middle of the bandgap, indicating moderately n-type conductivity; this can be seen from the intersection point of these defects in Fig. 4. While Zn_{In} creates one shallow acceptor level ε (0/-1) = 0.56 eV, In_{7n} creates one shallow donor level ε (0/-1) = 2.49 eV (both values measured from the VBM). DFE plots showing all native defects simulated from HSE06 are presented in Fig. S3, for S-rich conditions. It should be noted that similar types of cation-cation low energy anti-site substitutional defects have been reported in quaternary chalcogenides in Kesterite and Stannite phases, e.g., Cuzn and Cusn in Cu₂ZnSnS₄⁵¹.

Next, we examine the DFEs of all 172 SAC dopants (substitutional and interstitial) in terms of their E^f vs E_F behavior, energetic comparison with Zn_{In} and In_{Zn} , and location of defect levels. We perform screening of these SACs as shown in **Fig. 1(b)**, and find that 106 out of the 172 demonstrate higher stability than native defects under either In-rich or S-rich conditions, such that they will "dominate" over native defects and potentially tune

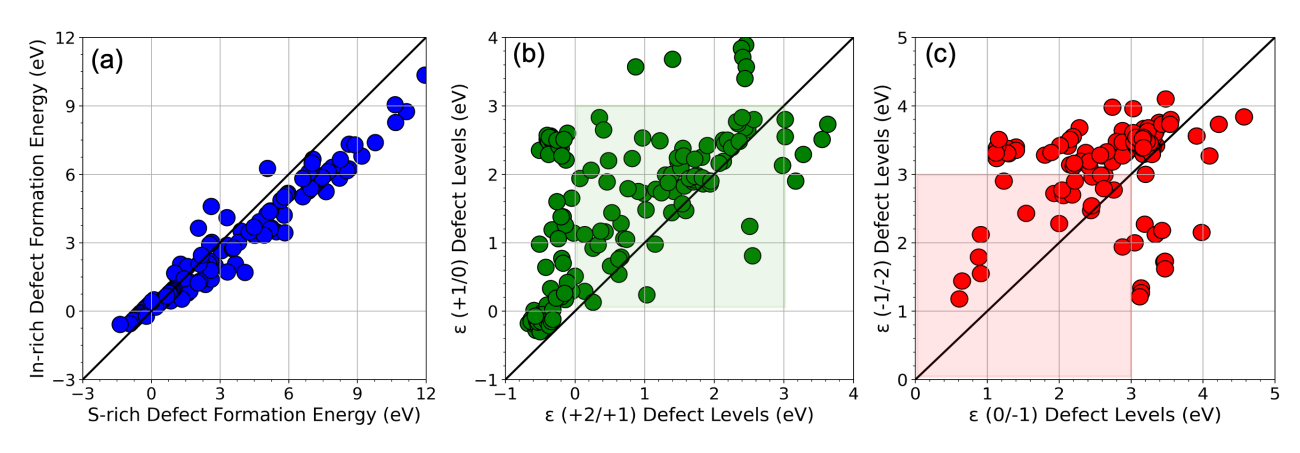


Fig. 2 Visualization of the HSE06 dataset: (a) Cation (In) vs anion (S) rich neutral defect formation energy, (b) ε (+2/+1) vs ε (+1/0) CTLs, and (c) ε (0/-1) vs ε (-1/-2) CTLs. The bandgap region is shaded in the CTL plots.

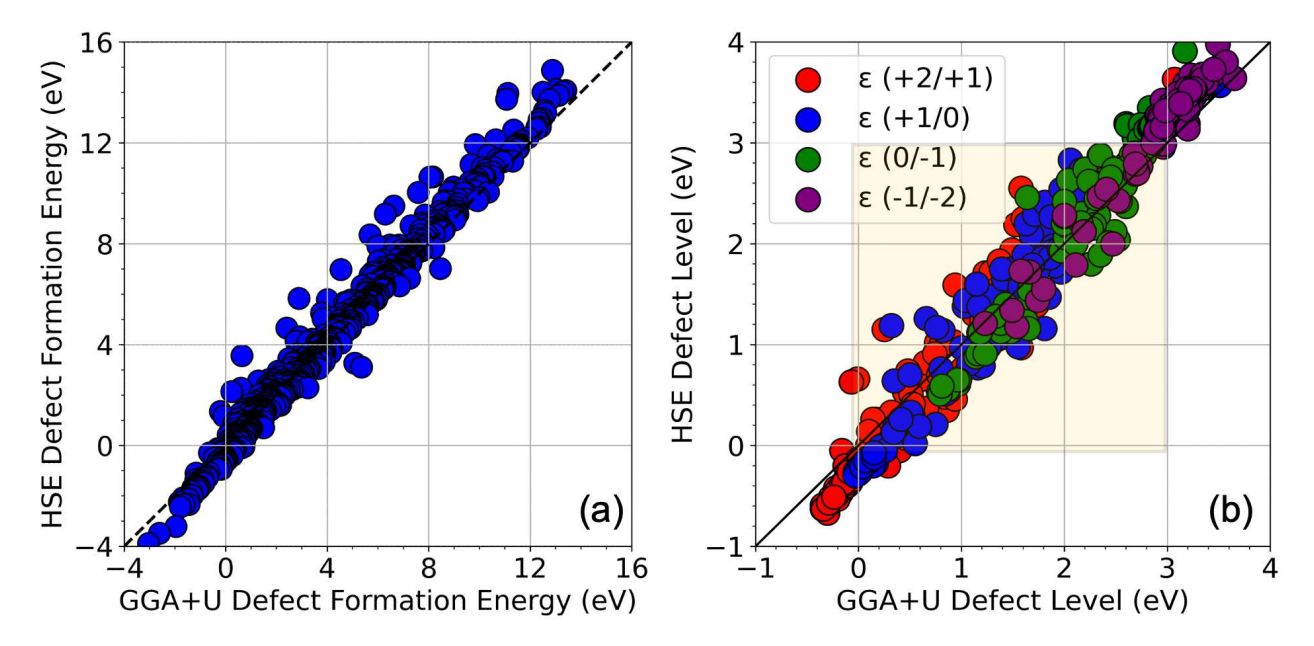


Fig. 3 (a) Comparison of defect formation energies from GGA+U and HSE06 for 5 charge states at the Fermi level = 0 (at the VBM). Only data points with DFE < 15 eV are pictured. (b) Comparison of different CTLs from GGA+U and HSE06. The bandgap region is shaded.

the equilibrium conductivity. A few examples of these low-energy SAC dopants are presented in **Table 1**, along with their lowest DFE values and the nature of defect levels in the bandgap. Out of the 106 dopants, we find that 60 display only shallow levels, i.e., they do not create any potentially harmful states deep within the bandgap. All of these defects are listed in **Table 2** along with their DFEs and relevant +1/0 or 0/-1 levels, as well as the type of charge state shown within the bandgap. A majority of these screened dopants are substitutional in nature rather than interstitials.

Although the CTLs for native defects and dopants in ZIS are not available experimentally for benchmarking

our calculated defect levels, it is important to note that our DFT predictions are based on well-established methodologies that have been shown to produce results in good agreement with measured defect levels in similar systems. Numerous studies have demonstrated that DFT calculations, when accompanied by the appropriate corrections (e.g., band edge, charge correction) and level of theories, can produce CTLs that are nearly equivalent to the experimentally obtained CTLs, as pictured in Fig. S4^{52,53}. We benchmarked defect levels for a variety of well-known binary semiconductors in past work⁵³, and as shown in Fig. S4(a), the root mean square errors between DFT and experiment are only around 0.2 eV. Fig. S4(b) further shows that computed defect levels for

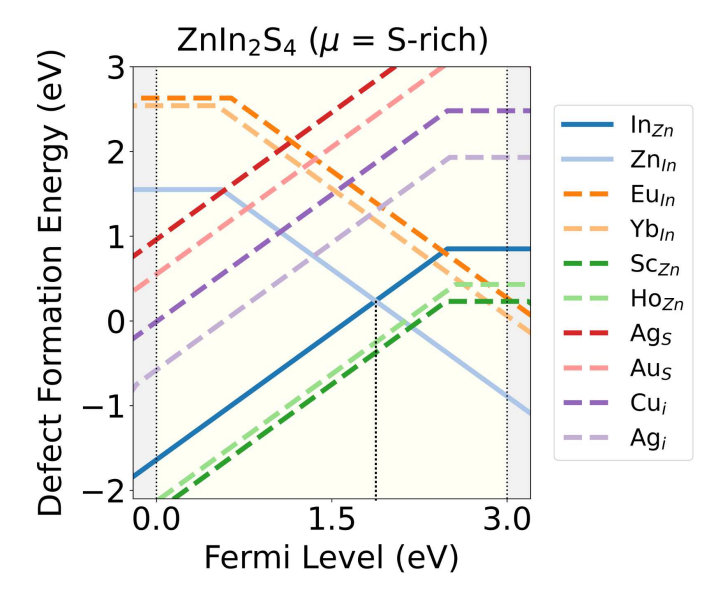


Fig. 4 Defect formation energeties of some notable SACs in ZIS with respect to lowest energy native acceptor (Zn_{ln}) and donor (In_{Zn}) defects under S-rich growth conditions, computed using HSE06. The equilibrium (E_F) as pinned by the native defects will be shifted to the right by Sc_{Zn} or Ho_{Zn} under these conditions.

transition metal dichalcogenides match quite well with experiments ⁵². The approaches used in this work, such as the selection of functionals and corrections, have been well-validated and used to give reasonable defect levels in various semiconductors. This gives us confidence in the accuracy of our CTL predictions for the systems being studied here.

8 out of the 60 promising dopants (Eu_{In}, Yb_{In}, Sc_{Zn}, Ho_{Zn}, Ag_S, Au_S, Cu_i and Au_i) are pictured in Fig. 4 in terms of their E^f plotted as a function of E_F , and in comparison with the lowest energy native acceptor (Zn_{In}) and donor (In_{Zn}) defects, under S-rich conditions. The reason behind choosing S-rich conditions is that typically, ZIS is synthesized via the solid-state reaction method, which involves reacting stoichiometric quantities of ZnS and In₂S₃ powders in a S-rich environment to inhibit oxidation under controlled conditions, thereby achieving the desired composition and crystalline structure. We observe that Sc_{Zn} and Ho_{Zn} are very low-energy donors and remain stable in p-type conditions while compensating for In_{Zn}. Eu_{In} and Yb_{In} are acceptor type defects that become stable in n-type conditions, whereas Ags, Aus, Cui and Agi are donors that are stable in p-type conditions. It should be noted that low energy dopants are determined on the basis of whether they dominate over the native defects under S-rich or In-rich conditions, even though only 2 of the 8 dopants pictured in Fig. 4 are actually dominating under S-rich conditions.

Next, we performed a statistical analysis to understand the correlation between fundamental properties of the SAC cations and the HSE06-computed defect properties, specifically for substitutional dopants. Fig. 5 shows the Pearson coefficients of linear correlation between 5 properties (neutral state DFE, $\varepsilon(+2/+1)$, $\varepsilon(+1/0)$, $\varepsilon(0/-1)$, and $\varepsilon(-1)$ 1/-2)) and well-known elemental properties (specifically, the difference between the property of the SAC dopant and the atom it is substituting: Zn, In, or S). These properties include the atomic number, atomic weight, boiling point, density, electron affinity, electronegativity, heat of fusion, heat of vaporization, ionization energy, ionic radius, melting point and period. We find that the DFE is notably positively correlated with $\Delta Elec$ Aff, $\Delta Electronegativity,$ Δ BP, Δ Heat vap, Δ Ion Energy, Δ Ion rad, and Δ Period. As the electron affinity and electronegativity difference between the host atom and dopant decreases, the DFE also goes down. $\varepsilon(+2/+1)$ shows some correlation with Δ Elec Aff and Δ BP, while (+1/0) defect level is highly correlated with AIon Energy, because the ionization energy determines the electron transfer necessary for the +1/0 transition. $\varepsilon(0/-1)$ shows some correlation with Δ Elec Aff for the same reasons, while $\varepsilon(-1/-2)$ does not show any notable correlations.

The correlations between different elemental descriptors and the computed defect properties help us understand some underlying physical mechanisms driving the behavior of the SACs. For instance, a SAC with a higher electron affinity would be able to collect more of the photogenerated electrons and use these to drive the HER. On the other hand, if the electron affinity of the SAC is too high or too low compared to that of the ZIS matrix, it could either overly stabilize the electrons, preventing their participation in the reaction, or fail to capture them effectively, both of which would reduce catalytic efficiency. The observed positive relationship between DFE and electron affinity (i.e., the difference in electron affinity between the SAC and host site of ZIS such as Zn, In, or S) indicates that the SACs with electron affinities not matching the host site in ZIS are likely to be unstable. This correlation highlights the delicate balance required in choosing SACs that can not only integrate well into the ZIS structure but also maintain high catalytic activity without compromising stability. Furthermore, the notable correlations between defect CTLs and the ionization energy and electron affinity were noted in our past work⁵⁴, as these properties directly determine the ability to accept or donate electrons.

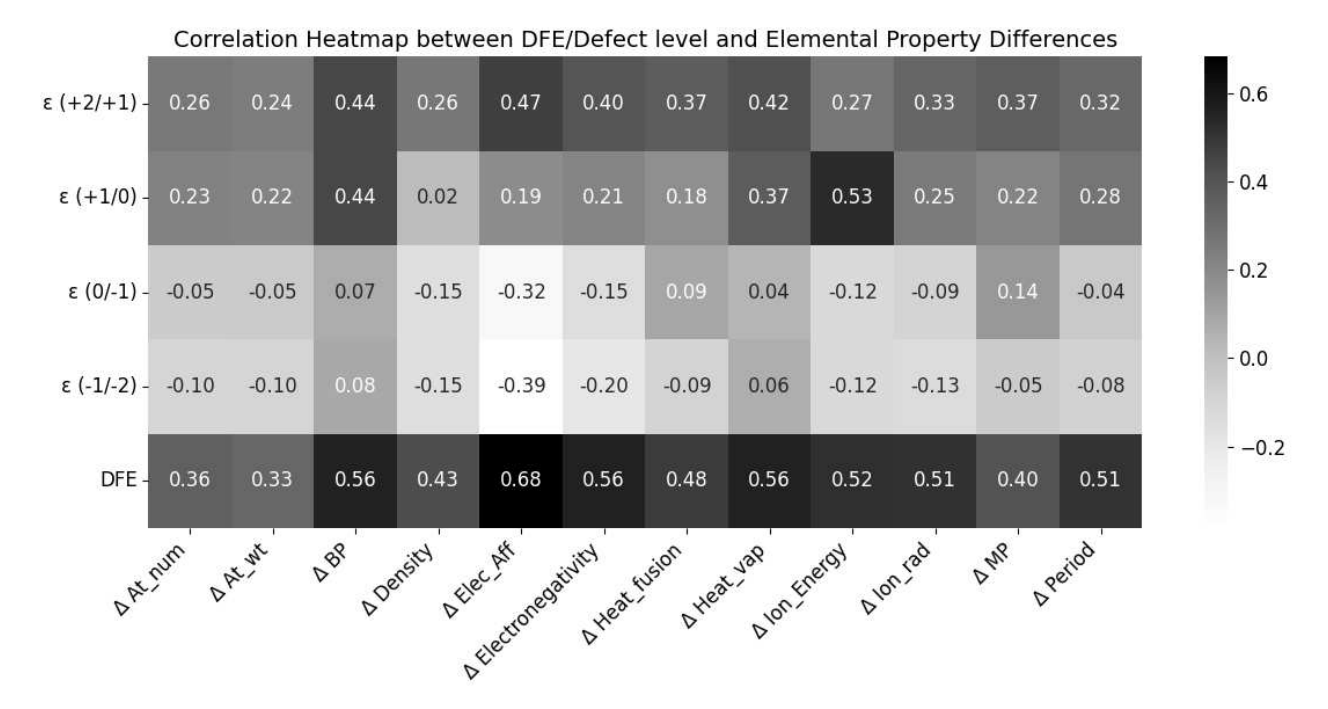


Fig. 5 Pearson correlation heatmap illustrating the relationship between defect levels $(\varepsilon(+2/+1), \varepsilon(+1/0), \varepsilon(0/-1), \varepsilon(-1/-2))$, defect formation energy (DFE), and the differences in elemental properties of the dopant relative to the host site atom.

Table 1 Some stable SACs with their lowest defect formation energy (DFE) at any particular E_{F} inside the bandgap, as well as their shallow or deep nature.

SACs	DFE (eV)	Nature
La _{Zn}	-1.54	Shallow
Ta_{In}	-1.47	Shallow
V_{In}	-1.34	Deep
Eu_i	-1.20	Shallow
Nb_{In}	-1.14	Deep
V_{Zn}	-1.05	Deep
Lu_{In}	-0.93	Shallow
Sc_{In}	-0.89	Shallow
Fe_{Zn}	-0.88	Deep
Yb _i	-0.84	Shallow

3.3 Photocatalytic Hydrogen Evolution Reaction (HER)

In this section, we explore the effect of the SACs on the photocatalytic HER performance of ZIS-free surfaces; a rough illustration of the process is shown in **Fig. 6(a)**. In an acidic environment, HER typically involves four key steps: the binding of H⁺ to active sites, the reduction of H⁺ through electron transfer, the formation of an adsorbed intermediate H^{*}, and the subsequent release of molecular H₂. A crucial factor in evaluating the effectiveness of the HER process is the Gibbs free energy difference $|\Delta G|$ associated with H adsorption. In this study, we estimate $|\Delta G|$ using the following equation: $|\Delta G| = E(ZIS +$

H) - E(ZIS) - $0.5H_2$ + (Δ ZPE - T Δ S). ZPE is calculated using ZPE = $\frac{1}{2}\sum hv_i$, where v_i denotes the vibrational frequency of either free H₂ placed in a large simulation box or H species adsorbed on the catalyst. When the vibrational frequency of the adsorbed H species is being computed, the entire catalyst structure (ZIS) is kept fixed, allowing the H atoms to vibrate freely in all directions. The entropy S is calculated using the following equation:

$$S(T) = \sum_{i=1}^{3N} \left[-R \ln \left(1 - e^{-\frac{hv_i}{K_B T}} \right) + \frac{N_A hv_i}{T} \frac{e^{-\frac{hv_i}{K_B T}}}{1 - e^{-\frac{hv_i}{K_B T}}} \right].$$
 For a

highly efficient HER catalyst, the ideal value of $|\Delta G|$ is zero. The HER process faces challenges when $|\Delta G|$ is excessively positive or excessively negative. In the former case, the adsorption of H^* on the catalyst surface is hindered while in the latter, the desorption of H^* from the catalyst surface is impeded.

We calculated the HER $|\Delta G|$ values for the 60 promising SAC candidates identified via DFT screening, which are listed in **Table S1**. In previous work, our computations showed that a Zn_i defect in ZIS lowers the HER $|\Delta G|$ as compared to pristine ZIS³⁷. Out of the 60 SACs, we find that Co_{In} , Yb_i , Tc_{Zn} , Au_s , La_i , Eu_i , Au_i , Ta_{In} , Hf_{In} , Zr_{In} , and Ni_{Zn} show lower $|\Delta G|$ than Zn_i , as presented in **Fig. 6(b)**. This improvement can be attributed to the modified electronic structure and the creation of localized states within the bandgap due to the introduction of defects. These defect states can potentially increase both the carrier

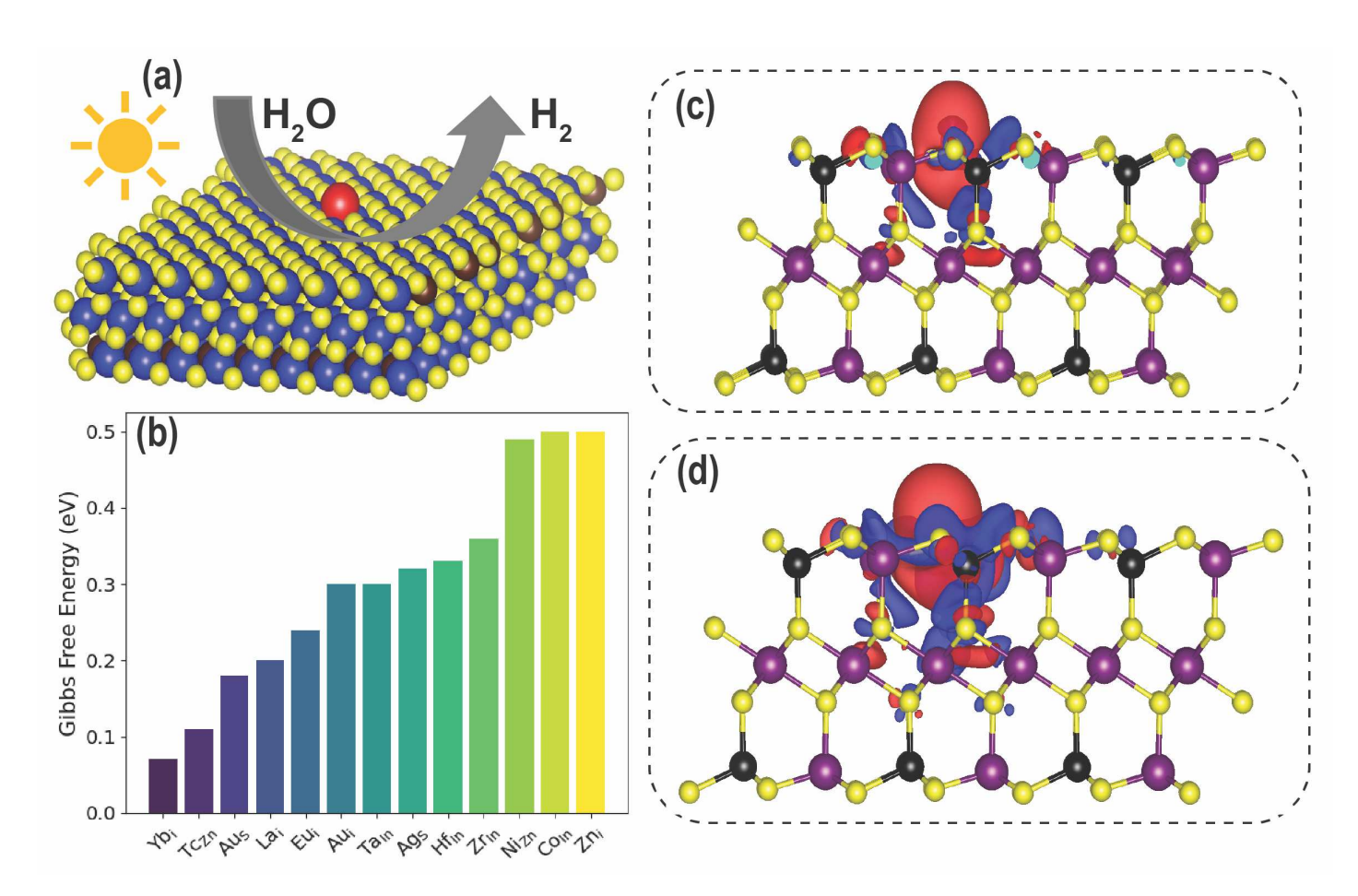


Fig. 6 (a) Illustration of the photocatalytic HER on the surface of SAC doped ZIS (b) Comparison of Gibbs free energy (ΔG) for pristine ZIS, and screened SACs such as Co_{In} , Yb_i , Tc_{Zn} , Au_S , La_i , Eu_i , Ag_S , Au_i , Ta_{In} , Hf_{In} , Zr_{In} , Ni_{Zn} and charge density difference (CDD) analysis of (c) ZIS and (d) Yb_i system.

concentration and electronic conductivity. Additionally, defects may introduce new catalytically active sites or enhance the adsorption of reactants, thereby further enhancing photocatalytic performance.

To gain more understanding of the charge transfer mechanism between the catalyst and H atom, we analyzed the charge density difference (CDD) between ZIS and H, as well as between Yb_i and H, as shown in **Fig. 6(c-d)**. Due to the introduction of Yb_i, the electronic structure is altered and conductivity is bolstered. Consequently, there is more charge transfer between the catalyst and H, which turns into stronger adsorption. These findings highlight the potential of tailored doping strategies for optimizing photocatalytic activity in ZIS. We note that enhancement in photocatalytic activity of Yb-doped TiO₂ has been substantiated through experimental investigations 55 , which further motivates experimental investigation of Yb-doped ZIS for photocatalysis.

Although ΔG is a key indicator of how efficiently a

photocatalyst can facilitate the HER, to understand the practical overall photocatalytic efficiency, several factors must be taken into account. For example, SACs based on noble metals may be expensive and result in increased cost of the photocatalytic system. While SACs could improve HER, they may also open routes for new reaction pathways or interfere with other photocatalytic reactions such as oxygen evolution. This could potentially lower the overall selectivity for hydrogen production and may need to be fine-tuned to optimize these effects. As our calculations of Gibbs free energy suggest, while there is a large potential for improvement of HER activity, translating these theoretical improvements into practical photocatalytic efficiency requires considering the overall system performance, including potential trade-offs. The potential increase in solar-to-hydrogen efficiency and the durability of photocatalysts is encouraging; however, there are other aspects that should also be considered, including cost, synthesis difficulty, and selectivity.

To understand the dynamic stability of the SAC-

Table 2 A list of stable and shallow-level SAC dopants, showing their lowest defect formation energy (DFE) at any particular E_F inside the bandgap as well as their selected defect levels references to the VBM.

Defects	DFE (eV)	ε (+1/0)	ε (0/-1)	Туре
Sc _{In}	-0.89	-	-	Neutral
$\mathrm{Ti}_{\mathrm{In}}$	-0.82	2.35	-	Donor
Co_{In}	1.35	0.29	2.46	Amphoteric
Y_{In}	-0.61	-	-	Neutral
Zr_{In}	-2.38	2.45	-	Donor
Cd_{In}	1.55	-	0.53	Acceptor
La _{In}	-0.07	-	-	Neutral
Ce_{In}	-0.54	-	-	Neutral
Pr_{In}	-0.14	-	-	Neutral
Nd_{In}	-0.2	-	-	Neutral
Pm_{In}	-0.26	-	-	Neutral
Sm_{In}	-0.33	-	-	Neutral
Eu_{In}	1.55	-	0.65	Acceptor
$\mathrm{Gd}_{\mathrm{In}}$	-0.46	-	-	Neutral
Tb_{In}	-0.52	-	-	Neutral
$\mathrm{Dy}_{\mathrm{In}}$	-0.59	-	-	Neutral
Ho_{In}	-0.66	-	-	Neutral
Er_{In}	-0.71	-	-	Neutral
Tm_{In}	-0.79	-	-	Neutral
Yb_{In}	1.55	-	0.51	Acceptor
$\mathrm{Lu}_{\mathrm{In}}$	-0.93	-	-	Neutral
Hf_{In}	-3.92	2.51	-	Donor
Ta_{In}	-1.47	2.43	-	Donor
Hg_{In}	1.4	-	0.59	Acceptor
Sc_{Zn}	-2.3	2.47	-	Donor
Mn_{Zn}	1.14	2.38	2.96	Amphoteric
Ni_{Zn}	1.08	0.21	2.3	Amphoteric
Y_{Zn}	-2.13	2.55	-	Donor
Tc_{Zn}	0.27	2.83	-	Donor
$\mathrm{Cd}_{\mathrm{Zn}}$	-0.22	-	-	Neutral
La_{Zn}	-1.54	2.47	-	Donor
Ce_{Zn}	-0.4	2.43	-	Donor
Pr_{Zn}	-1.68	2.55	-	Donor
Nd_{Zn}	-1.75	2.56	-	Donor
Pm_{Zn}	-1.83	2.57	-	Donor
Sm_{Zn}	-1.74	2.43	-	Donor
Eu_{Zn}	0.78	-	-	Neutral
$\operatorname{Gd}_{\operatorname{Zn}}$	-1.89	2.46	-	Donor
Tb_{Zn}	-2.01	2.53	-	Donor
$\mathrm{Dy}_{\mathrm{Zn}}$	-2.04	2.48	-	Donor
Ho_{Zn}	-2.18	2.56	-	Donor
$\operatorname{Er}_{\operatorname{Zn}}$	-2.17	2.5	-	Donor
Tm_{Zn}	-2.17	2.42	-	Donor
Yb_{Zn}	0.67	-	-	Neutral
Lu_{Zn}	-2.38	2.51	-	Donor
Hg_{Zn}	-0.24	-	-	Neutral
Ag_S	0.91	2.41	-	Donor
Au_S	0.5	2.54	-	Donor
Cu _i	-0.06	2.5	-	Donor
Y_i	0.74	2.68	-	Donor
Agi	-0.63	2.51	-	Donor
La _i	0.34	0.26	-	Donor
Nd _i	0.64	-	-	Donor
Eui	-1.2	2.8	-	Donor
Gd _i	0.72	2.48	-	Donor
Tm _i	0.61	2.77	2.57	Amphoteric
Yb _i	-0.84	2.83	-	Donor
Hf _i	1.4	2.55	-	Donor
10 Au _i	0.17	2 . 27	-	Donor
Hg _i	0	0.26	-	Donor

containing ZIS compounds and to evaluate their performance under conditions close to operating temperatures, we performed ab initio molecular dynamics (AIMD) simulations at 300 K for a chosen SAC, Ybi. During AIMD, the temperature of the system is maintained using a Nosé-Hoover thermostat under the NVT ensemble³⁷. This simulation was run for a total of 2 ps using a 1 fs time step. The results indicate that ZIS with Ybi maintains its structural integrity throughout the simulation, as depicted in Fig. S5, demonstrating its dynamic stability. The total energy remains roughly constant, and the structure snapshots at different times appear nearly identical. A movie showing the dynamics is included in the SI as an MP4 file. We further computed the velocity autocorrelation function (VACF) from the AIMD trajectories, which quantifies how the velocity of an atom at a given time is correlated with its velocity at a later time. Mathematically, it is expressed as⁵⁶:

$$C_{\nu}(t) = \frac{1}{N} \sum_{i=1}^{N} \langle \mathbf{v}_{i}(0) \cdot \mathbf{v}_{i}(t) \rangle$$
 (3)

Here, $C_v(t)$ is the velocity autocorrelation function at time t, N is the total number of atoms in the system, $\mathbf{v}_i(0)$ is the velocity of atom i at time t = 0, $\mathbf{v}_i(t)$ is the velocity of atom i at time t, and $\langle \cdot \rangle$ represents the ensemble average over time or multiple configurations. We then computed the vibrational density of states (VDOS) from the VACF, which represents the distribution of vibrational modes over frequencies in a system. To compute the VDOS from the VACF, we applied the Fast Fourier Transform (FFT), which transforms the time-domain data (VACF) into the frequency domain. The VDOS, $g(\omega)$, is computed as:

$$g(\omega) = \int_{-\infty}^{\infty} C_{\nu}(t)e^{-i\omega t}dt \tag{4}$$

Here, $g(\omega)$ is the VDOS at frequency ω , $C_{\nu}(t)$ is the velocity autocorrelation function, and $e^{-i\omega t}$ is the exponential factor in the Fourier transform, which relates time-domain data to frequency-domain data. Peaks in the VDOS correspond to dominant vibrational modes, as pictured in Fig. S5(c), and the absence of significant low-frequency modes suggests dynamic stability since low-frequency or zero-frequency modes often indicate structural instability. This finding reinforces our earlier conclusions regarding the suitability of Yb_i as an effective and stable SAC in photocatalytic applications.

Beyond the results discussed so far, it is also important to determine the stability of SACs under operating conditions, particularly during the HER process, especially because single atoms could potentially aggregate into larger particles. To confirm the stability of Yb_i on the ZIS surface, we used the nudged elastic band (NEB) method to simulate the migration of Yb on the surface, as shown in Fig. S6(a). As shown in Fig. S6(b), our calculations revealed a very high migration energy barrier for Yb (~ 1.01 eV), meaning the Yb_i SAC is unlikely to hop or segregate from the ZIS surface. Furthermore, we computed the DFE for an increasing number of Yb atoms on ZIS, going from single Yb_i to double, triple, and quadruple defects, as pictured in Fig. S6(c). We found a steady increase in the DFE with Yb atoms, as shown in Fig. S6(d), which indicates that accommodating multiple Yb_i is quite energetically unfavorable and that Yb_i is stable and non-aggregative, and will remain as discrete single atoms without forming any clusters. This is important in maintaining the catalytic activity of Yb, during HER as it prevents the loss of active sites due to aggregation. However, it should be noted that clusters of atoms (if energetically favorable) could improve catalytic activity compared to single atoms in some cases ^{57,58}.

4 Conclusions

In this study, we performed high-throughput density functional theory (DFT) computations to explore the potential of single-atom co-catalysts (SACs) in improving the photocatalytic performance of ZnIn₂S₄ (ZIS). Our focus was on transition metals from the 3d, 4d, and 5d series, as well as lanthanides, considering both substitutional and interstitial doping sites. A total of 172 SACs were considered and their defect formation energy (DFE) was computed as a function of chemical potential, charge state, and Fermi level ($E_{\rm F}$). Our analysis identified 60 SACs with lower DFEs than the dominant native defects in ZIS and only shallow defect levels within the bandgap. Notably, SACs such as Co_{In}, Yb_i, Tc_{Zn}, Au_S, La_i, Eu_i, Au_i, Ta_{In}, Hf_{In}, Zr_{In}, and Ni_{Zn} demonstrated lower Gibbs free energy for HER compared to previously studied pristine ZIS or ZIS with Zn_i. This improvement is attributed to the introduction of defect states that enhance carrier concentration and electronic conductivity. The potential of Yb-doped ZIS for photocatalysis is further supported by experimental evidence of enhanced photocatalytic activity in Yb-doped TiO₂. Overall, our computational workflow, dataset, and insights provide motivation for the experimental design of novel SACs in ZIS. The identified low-energy SACs offer new avenues for optimizing photocatalytic properties, promising significant advancements in environmental remediation applications.

Conflicts of Interest

There are no conflicts to declare.

Data Availability

All data is available in spreadsheets as part of the Supporting Information.

Acknowledgements

A. M. K. acknowledges funding from the National Science Foundation (CHE-1955336) and support from the School of Materials Engineering at Purdue University. Y. S. acknowledges the support of the National Science Foundation (CHE-1955358). This research used resources from the Rosen Center for Advanced Computing (RCAC) clusters at Purdue University.

References

- 1 S. Wang, Z. Ding, X. Chang, J. Xu and D.-H. Wang, *Catalysts*, 2020, **10**, 759.
- 2 X. Chang, G. Yu, J. Huang, Z. Li, S. Zhu, P. Yu, C. Cheng, S. Deng and G. Ji, *Catalysis Today*, 2010, **153**, 193–199.
- 3 C. Han, G. Han, M. H. Rahman, A. Mannodi-Kanakkithodi and Y. Sun, *Chemistry a European Journal*, 2023, **29**, 202203785.
- 4 A. Singh, B. Yuan, M. H. Rahman, H. Yang, A. De, J. Y. Park, S. Zhang, L. Huang, A. Mannodi-Kanakkithodi, T. J. Pennycook and L. Dou, *Journal of the American Chemical Society*, 2023, 145, 19885–19893.
- 5 A. FUJISHIMA and K. HONDA, *Nature*, 1972, **238**, 37–38.
- 6 X. Shi, L. Mao, P. Yang, H. Zheng, M. Fujitsuka, J. Zhang and T. Majima, Applied Catalysis B: Environmental, 2020, 265, 118616.
- 7 U. Alam, M. Fleisch, I. Kretschmer, D. Bahnemann and M. Muneer, *Applied Catalysis B: Environmental*, 2017, **218**, 758–769.
- 8 J. Wang, S. Sun, R. Zhou, Y. Li, Z. He, H. Ding, D. Chen and W. Ao, *Journal of Materials Science Technology*, 2021, **78**, 1–19.
- 9 J. Low, B. Cheng and J. Yu, *Applied Surface Science*, 2017, **392**, 658–686.
- 10 G. Zhang, H. Wu, D. Chen, N. Li, Q. Xu, H. Li, J. He and J. Lu, *Green Energy Environment*, 2022, 7, 176–204.
- 11 J. Chen, F. Xin, X. Yin, T. Xiang and Y. Wang, *RSC Advances*, 2015, **5**, 3833–3839.
- 12 P. Wang, Z. Shen, Y. Xia, H. Wang, L. Zheng, W. Xi and S. Zhan, *Advanced Functional Materials*, 2018, **29**, 1807013.
- 13 G. Han, X. Liu, Z. Cao and Y. Sun, *ACS Catalysis*, 2020, **10**, 9346–9355.
- 14 C. Du, Q. Zhang, Z. Lin, B. Yan, C. Xia and G. Yang, *Applied Catalysis B: Environmental*, 2019, **248**, 193–201.
- 15 Y. Chen, R. Huang, D. Chen, Y. Wang, W. Liu, X. Li

- and Z. Li, ACS Applied Materials Interfaces, 2012, 4, 2273–2279.
- 16 Y. J. Zhang, H. M. Tang and S.-P. Gao, physica status solidi (b), 2019, 257, 1900485.
- 17 Z. Zafar, S. Yi, J. Li, C. Li, Y. Zhu, A. Zada, W. Yao, Z. Liu and X. Yue, *ENERGY ENVIRONMENTAL MATERIALS*, 2021, **5**, 68–114.
- 18 D. Maarisetty and S. S. Baral, *Journal of Materials Chemistry A*, 2020, **8**, 18560–18604.
- 19 W.-K. Chong, B.-J. Ng, C.-C. Er, L.-L. Tan and S.-P. Chai, *Scientific Reports*, 2022, **12**, 1927.
- 20 H. J. Queisser and E. E. Haller, *Science*, 1998, **281**, 945–950.
- 21 D. Wang, X.-B. Li, D. Han, W. Q. Tian and H.-B. Sun, *Nano Today*, 2017, **16**, 30–45.
- 22 D. Lee, J.-W. Park, N.-K. Cho, J. Lee and Y. S. Kim, *Scientific Reports*, 2019, **9**, 10323.
- 23 M. Kumar, P. Basera, S. Saini and S. Bhattacharya, *The Journal of Physical Chemistry C*, 2020, **124**, 10272–10279.
- 24 X. Jing, N. Lu, J. Huang, P. Zhang and Z. Zhang, *Journal of Energy Chemistry*, 2021, **58**, 397–407.
- 25 C. Foo, Y. Li, K. Lebedev, T. Chen, S. Day, C. Tang and S. C. E. Tsang, *Nature Communications*, 2021, **12**, 661.
- 26 F. G. Sen, A. Mannodi-Kanakkithodi, T. Paulauskas, J. Guo, L. Wang, A. Rockett, M. J. Kim, R. F. Klie and M. K. Chan, *Solar Energy Materials and Solar Cells*, 2021, 232, 111279.
- 27 Y. Niu, C. Yue, S. Li, G. Che, N. Su, H. Dong and C. Li, *Carbon Letters*, 2023.
- 28 Y. Zhang, J. Zhao, H. Wang, B. Xiao, W. Zhang, X. Zhao, T. Lv, M. Thangamuthu, J. Zhang, Y. Guo, J. Ma, L. Lin, J. Tang, R. Huang and Q. Liu, *Nature Communications*, 2022, **13**, 58.
- 29 S. Hejazi, M. S. Killian, A. Mazare and S. Mohajernia, *Catalysts*, 2022, **12**, 905.
- 30 C. Li, W. Pan, Z. Zhang, T. Wu and R. Guo, *Small*, 2023, **19**, 2300460.
- 31 Y. Peng, B. Lu and S. Chen, *Advanced Materials*, 2018, **30**, 1870370.
- 32 Z.-H. Xue, D. Luan, H. Zhang and X. W. (David) Lou, *Joule*, 2022, **6**, 92–133.
- 33 A. Martí, E. Antolín, C. R. Stanley, C. D. Farmer, N. López, P. Díaz, E. Cánovas, P. G. Linares and A. Luque, *Physical Review Letters*, 2006, 97, 247701.
- 34 A. Luque and A. Martí, *Physical Review Letters*, 1997, **78**, 5014–5017.
- 35 L. Du, Y. Sun and B. You, *Materials Reports: Energy*, 2021, **1**, 100004.

- 36 X. Shi, C. Dai, X. Wang, J. Hu, J. Zhang, L. Zheng, L. Mao, H. Zheng and M. Zhu, *Nature Communications*, 2022, 13, 1287.
- 37 M. H. Rahman, J. Yang, Y. Sun and A. Mannodi-Kanakkithodi, *Surfaces and Interfaces*, 2023, **39**, 102960.
- 38 A. Mannodi-Kanakkithodi, J.-S. Park, A. B. F. Martinson and M. K. Y. Chan, *The Journal of Physical Chemistry C*, 2020, **124**, 16729–16738.
- 39 G. Kresse and J. Furthmüller, *Physical Review B*, 1996, **54**, 11169–11186.
- 40 J. P. Perdew, K. Burke and M. Ernzerhof, *Physical Review Letters*, 1996, 77, 3865–3868.
- 41 P. E. Blöchl, *Physical Review B*, 1994, **50**, 17953–17979.
- 42 H. T. Mumu, A. Zaman, F. H. Bhuiyan, R. H. Aunkon and A. Sharif, *Micro and Nanostructures*, 2023, **174**, 207470.
- 43 A. Zaman, H. T. Mumu, R. H. Aunkon, F. H. Bhuiyan and A. Sharif, *Journal of Physics Communications*, 2022, **6**, 105007.
- 44 M. H. Rahman, P. Gollapalli, P. Manganaris, S. K. Yadav, G. Pilania, B. DeCost, K. Choudhary and A. Mannodi-Kanakkithodi, *APL Machine Learning*, 2024, **2**, 016122.
- 45 J. Zheng, C. Fan, X. Li, Q. Yang, D. Wang, A. Duan, J. Ding, S. Rong, Z. Chen, J. Luo and B. Zhang, *Chemical Engineering Journal*, 2022, 446, 137371.
- 46 C. Han, G. Han, S. Yao, L. Yuan, X. Liu, Z. Cao, A. Mannodi-Kanakkithodi and Y. Sun, *Advanced Science*, 2021, **9**, 2103408.
- 47 C. Freysoldt, B. Grabowski, T. Hickel, J. Neugebauer, G. Kresse, A. Janotti and C. G. Van De Walle, *Reviews of Modern Physics*, 2014, 86, 253–305.
- 48 A. Walsh, Npj Computational Materials, 2021, 7, 72.
- 49 A. Jain, S. P. Ong, G. Hautier, W.-W. Chen, W. D. Richards, S. Dacek, S. Cholia, D. Gunter, D. Skinner, G. Ceder and K. A. Persson, *APL Materials*, 2013, 1, 011002.
- 50 S. Yao, B. Anasori and A. Strachan, *Journal of Applied Physics*, 2022, **132**,.
- 51 J. S. Park, S. Kim, Z. Xie and A. Walsh, *Nature Reviews Materials*, 2018, **3**, 194–210.
- 52 J. Y. Kim, Gelczuk, M. P. Polak, D. Hlushchenko, D. Morgan, R. Kudrawiec and I. Szlufarska, *Npj 2D Materials and Applications*, 2022, **6**, 75.
- 53 A. Mannodi-Kanakkithodi, X. Xiang, L. Jacoby, R. Biegaj, S. T. Dunham, D. R. Gamelin and M. K. Chan, *Patterns*, 2022, **3**, 100450.
- 54 A. Mannodi-Kanakkithodi, M. Y. Toriyama, F. G. Sen, M. J. Davis, R. F. Klie and M. K. Y. Chan, *npj Computa*-

12 | 1

- tional Materials, 2020, 6, 39.
- 55 X. Jiang, C. Li, S. Liu, F. Zhang, F. You and C. Yao, *RSC Advances*, 2017, **7**, 24598–24606.
- 56 M. S. Islam, I. Mia, A. S. M. J. Islam, C. Stampfl and J. Park, *Scientific Reports*, 2022, **12**, 761.
- 57 L. Liu, T. Chen and Z. Chen, *Advanced Science*, 2024, **11**, 2308046.
- 58 L. Zhang, J. Yang, X. Yang, A. Wang and T. Zhang, *Chem Catalysis*, 2023, **3**, 100560.

Supplemental material to "High Throughput Screening of Single Atom Co-Catalysts in ZnIn₂S₄ for Photocatalysis"

Md Habibur Rahman, 1), Yujie Sun 2) and Arun Mannodi-Kanakkithodi 1, a)

¹School of Materials Engineering, Purdue University, West Lafayette, Indiana 47907, USA ²Department of Chemistry, University of Cincinnati, Cincinnati, OH 45221 USA

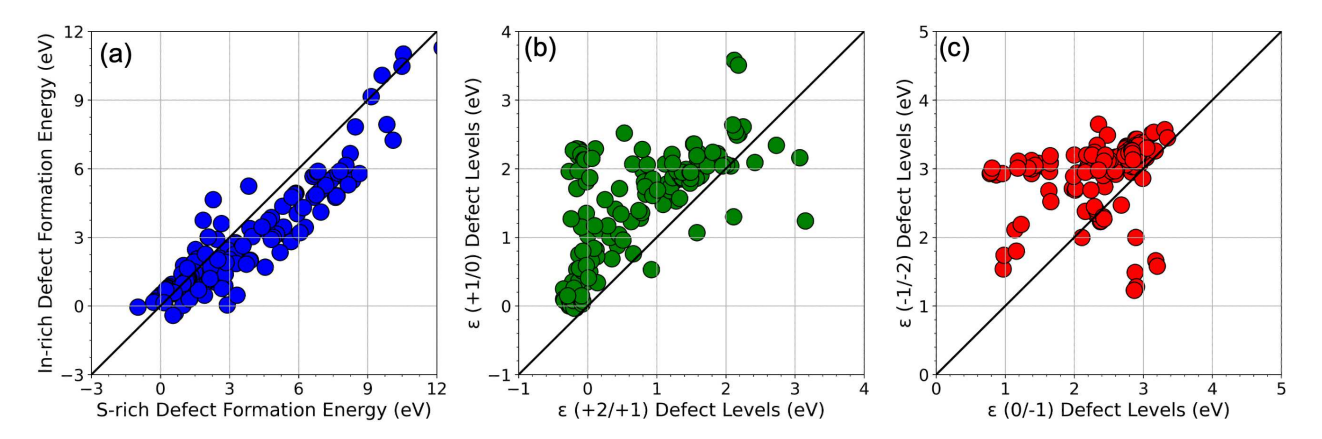


Fig. S1 Visualization of GGA+U DFT data—(a) Cation (In) vs anion(S) defect rich formation energy, (b) +2/+1 vs +1/0 and (c) 0/-1 vs -1/-2 defect levels.

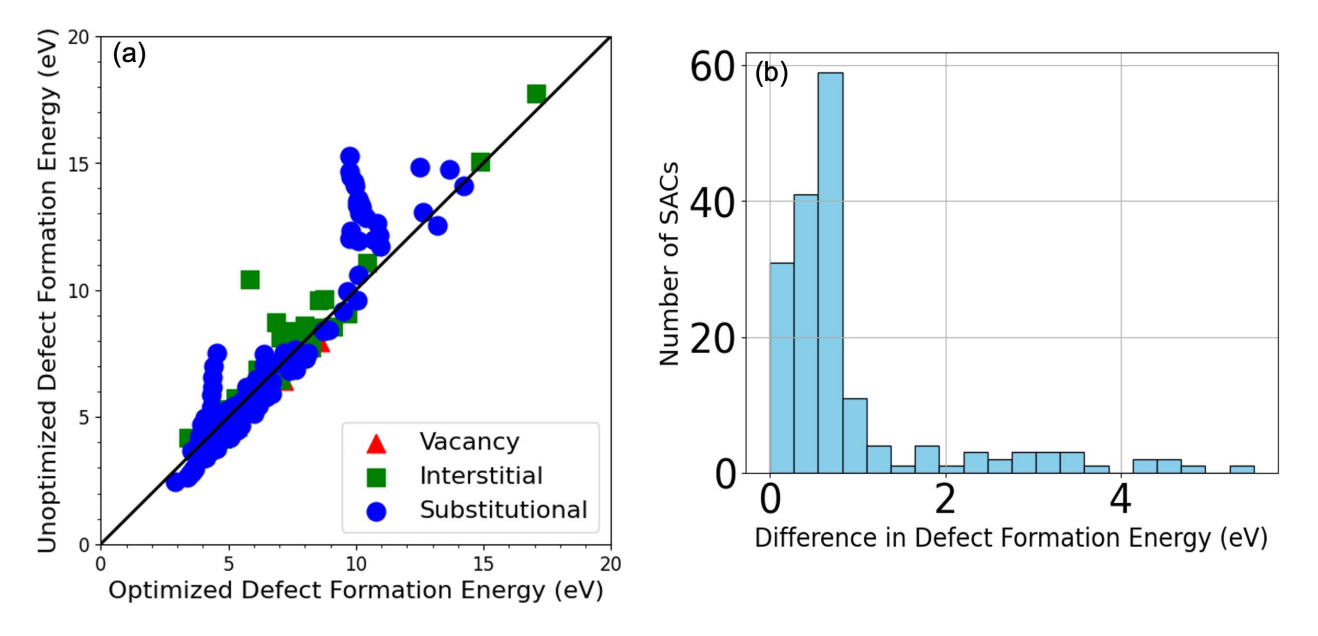


Fig. S2 (a) DFT optimized vs unoptimized defect formation energy (DFE) (b) Distribution of DFE difference (DFT optimized – DFT unoptimized) for SACs.

A Chemical Potential Expressions for SACs

^aamannodi@purdue.edu

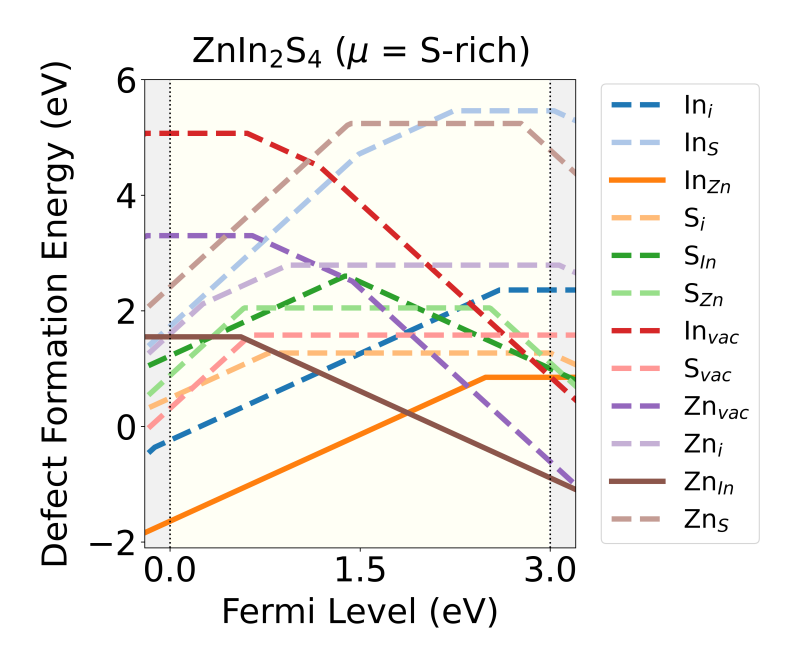


Fig. S3 DFE of all the native defects in ZIS as a function of E_F using HSE06 functional under S-rich conditions. The lowest energy donor and acceptor are depicted with solid line.

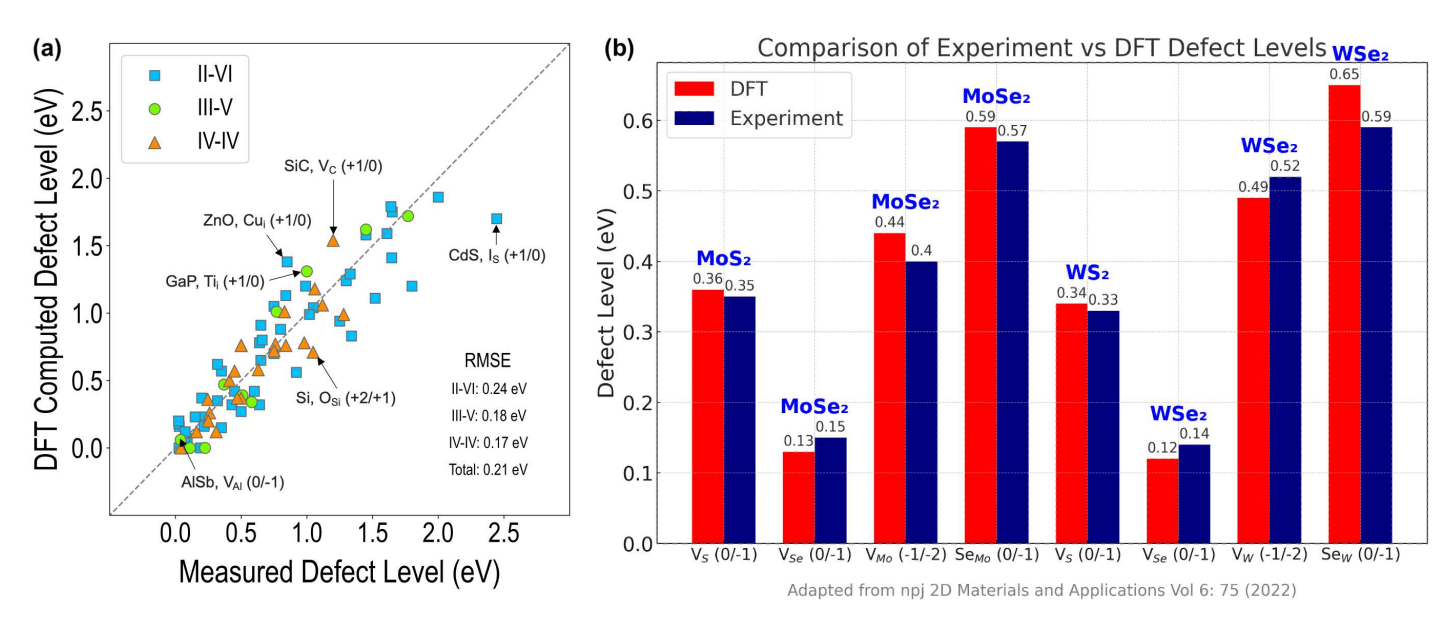


Fig. S4 Comparison of defect levels between DFT calculations and experimental observations for various (a) binary zinc blende (ZB) semiconductors and (b) transition metal dichalcogenide (TMDC) semiconductors. Collected from prior literature ^{52,53}. Permission to reuse Fig. S4(a) has been obtained from Elsevier.

$$\Delta\mu_{\rm Sc} + 2\Delta\mu_{\rm S} = \Delta H({\rm ScS}_2) \qquad \Delta\mu_{\rm Cr} + 2\Delta\mu_{\rm S} = \Delta H({\rm CrS}_2) \qquad \Delta\mu_{\rm Co} + 2\Delta\mu_{\rm S} = \Delta H({\rm CoS}_2)$$

$$\Delta\mu_{\rm Ti} + 2\Delta\mu_{\rm S} = \Delta H({\rm TiS}_2) \qquad \Delta\mu_{\rm Mn} + 2\Delta\mu_{\rm S} = \Delta H({\rm MnS}_2) \qquad \Delta\mu_{\rm Ni} + 2\Delta\mu_{\rm S} = \Delta H({\rm NiS}_2)$$

$$\Delta\mu_{\rm V} + 2\Delta\mu_{\rm S} = \Delta H({\rm VS}_2) \qquad \Delta\mu_{\rm Fe} + \Delta\mu_{\rm S} = \Delta H({\rm FeS}) \qquad \Delta\mu_{\rm Cu} + \Delta\mu_{\rm S} = \Delta H({\rm CuS})$$

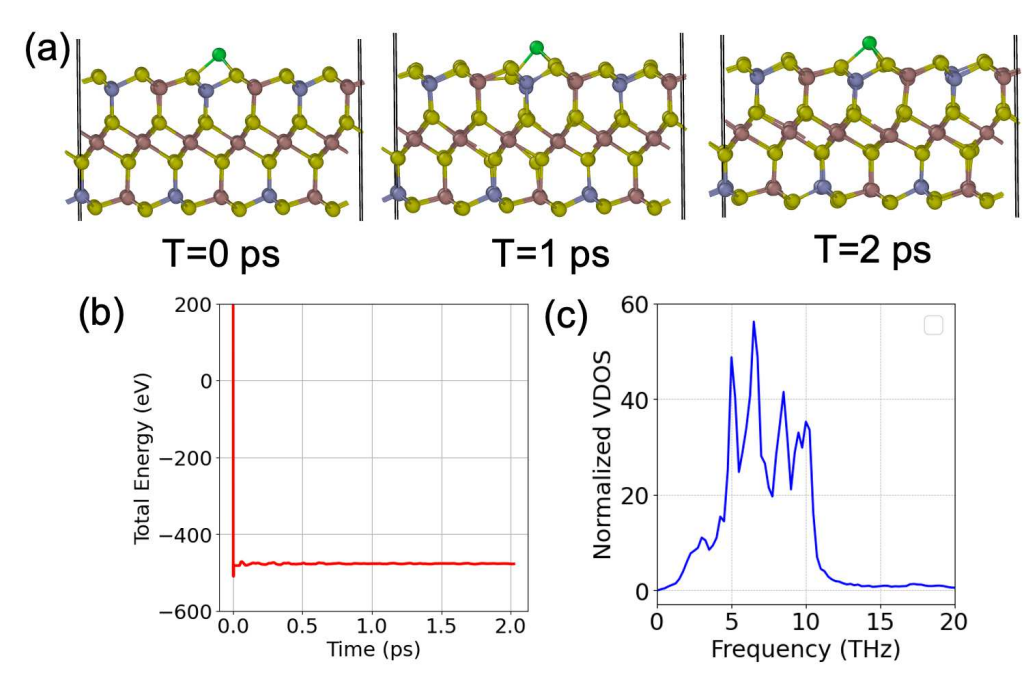


Fig. S5 (a) Snapshots of the crystal structure of Yb_i (green color) in ZIS during AIMD simulations at 300 K. (b) Energy profile during the AIMD simulation. (c) Normalized vibrational density of states (VDOS) for Yb_i in ZIS.

$\Delta\mu_{ m Y} + \Delta\mu_{ m S} = \Delta H({ m YS})$	$2\Delta\mu_{Ag} + \Delta\mu_{S} = \Delta H(Ag_{2}S)$	$\Delta\mu_{\mathrm{Dy}} + \Delta\mu_{\mathrm{S}} = \Delta H(\mathrm{DyS})$
$\Delta\mu_{\mathrm{Zr}} + \Delta\mu_{\mathrm{S}} = \Delta H(\mathrm{ZrS})$	$\Delta\mu_{\mathrm{Cd}} + \Delta\mu_{\mathrm{S}} = \Delta H(\mathrm{CdS})$	$\Delta \mu_{ m Ho} + \Delta \mu_{ m S} = \Delta H(m HoS)$
$\Delta\mu_{\mathrm{Nb}} + 3\Delta\mu_{\mathrm{S}} = \Delta H(\mathrm{NbS}_3)$	$\Delta \mu_{\mathrm{La}} + \Delta \mu_{\mathrm{S}} = \Delta H(\mathrm{LaS})$	$\Delta\mu_{\mathrm{Er}} + \Delta\mu_{\mathrm{S}} = \Delta H(\mathrm{ErS})$
An AMAN AMAN AMAN	$\Delta\mu_{Ce} + \Delta\mu_{S} = \Delta H(CeS)$	$\Delta\mu_{\mathrm{Tm}} + \Delta\mu_{\mathrm{S}} = \Delta H(\mathrm{TmS})$
$\Delta\mu_{Mo} + 2\Delta\mu_{S} = \Delta H(MoS_2)$	$\Delta\mu_{\mathrm{Pr}} + \Delta\mu_{\mathrm{S}} = \Delta H(\mathrm{PrS})$	$\Delta\mu_{\mathrm{Yb}} + \Delta\mu_{\mathrm{S}} = \Delta H(\mathrm{YbS})$
$\Delta\mu_{\mathrm{Tc}} + 2\Delta\mu_{\mathrm{S}} = \Delta H(\mathrm{TcS}_2)$	$\Delta\mu_{\mathrm{Nd}} + \Delta\mu_{\mathrm{S}} = \Delta H(\mathrm{NdS})$	$\Delta\mu_{\mathrm{Lu}} + \Delta\mu_{\mathrm{S}} = \Delta H(\mathrm{LuS})$
	$\Delta\mu_{\rm Pm} + \Delta\mu_{\rm S} = \Delta H({\rm PmS})$	
$\Delta\mu_{\mathrm{Ru}} + 2\Delta\mu_{\mathrm{S}} = \Delta H(\mathrm{RuS}_2)$	$\Delta\mu_{\rm Sm} + \Delta\mu_{\rm S} = \Delta H({\rm SmS})$	$2\Delta\mu_{\mathrm{Hf}} + \Delta\mu_{\mathrm{S}} = \Delta H(\mathrm{Hf_2S})$
$\Delta\mu_{\rm Rh} + 2\Delta\mu_{\rm S} = \Delta H({\rm RhS_2})$	$\Delta\mu_{\mathrm{Eu}} + \Delta\mu_{\mathrm{S}} = \Delta H(\mathrm{EuS})$	$3\Delta\mu_{\mathrm{Ta}} + 2\Delta\mu_{\mathrm{S}} = \Delta H(\mathrm{Ta}_{3}\mathrm{S}_{2})$
	$\Delta\mu_{\rm Gd} + \Delta\mu_{\rm S} = \Delta H({\rm GdS})$	

 $\Delta \mu_{\text{Tb}} + \Delta \mu_{\text{S}} = \Delta H(\text{TbS})$

 $\Delta\mu_{\rm W} + 2\Delta\mu_{\rm S} = \Delta H({\rm WS}_2)$

1-

 $\Delta\mu_{\mathrm{Pd}} + 2\Delta\mu_{\mathrm{S}} = \Delta H(\mathrm{PdS}_2)$

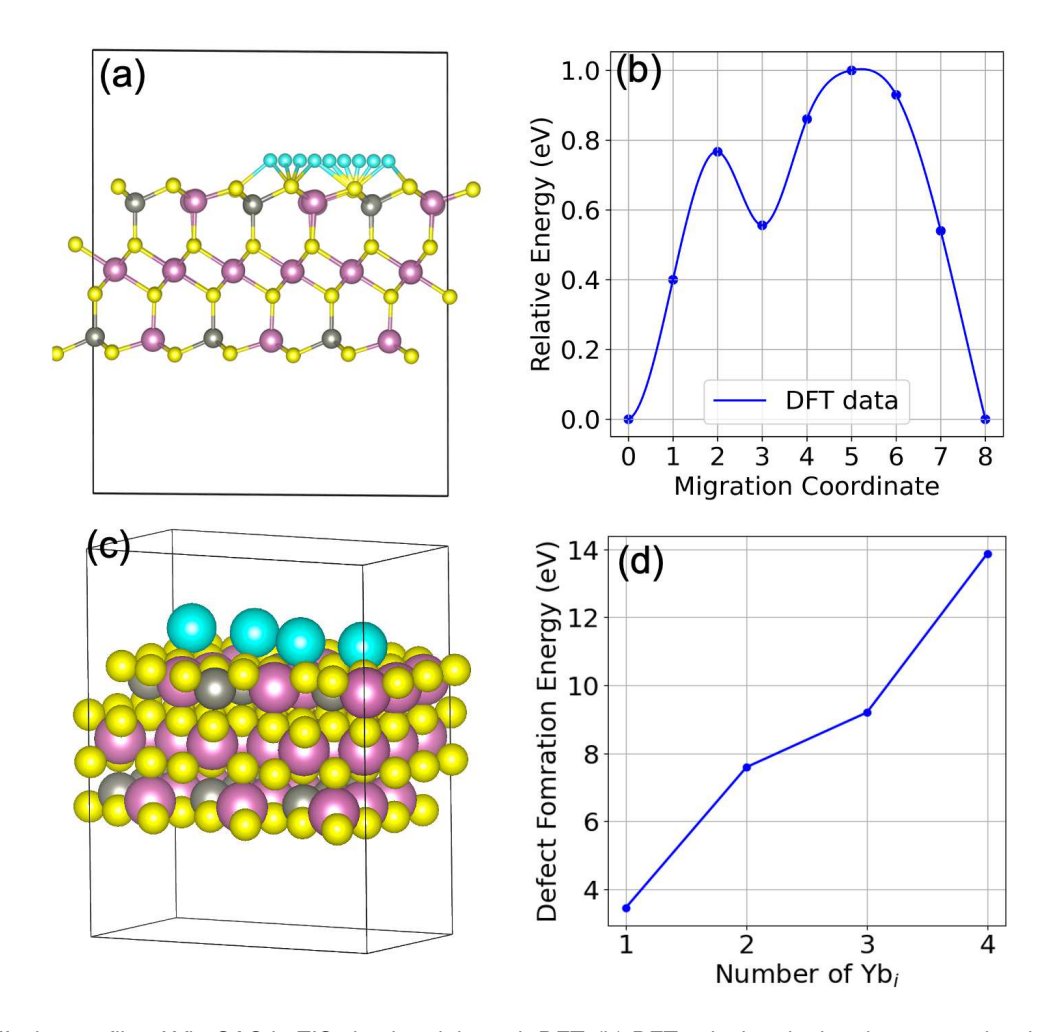


Fig. S6 (a) Diffusion profile of Yb_i SAC in ZIS simulated through DFT, (b) DFT calculated migration energy barrier of the same SAC as a function of migration coordinate, (c) cluster of Yb_i (quadruple) SACs in ZIS, (d) defect formation energy of single, double, triple, and quadruple SACs. Color scheme: In (Pink), Zn (Silver), S (Yellow), and Yb (Cyan).

$$\Delta\mu_{\rm Re} + 2\Delta\mu_{\rm S} = \Delta H({\rm ReS}_2)$$

$$2\Delta\mu_{\rm Au} + \Delta\mu_{\rm S} = \Delta H({\rm Au}_2{\rm S})$$

$$\Delta\mu_{\rm Os} + 2\Delta\mu_{\rm S} = \Delta H({\rm OsS}_2)$$

$$\Delta\mu_{\rm Pt} + 2\Delta\mu_{\rm S} = \Delta H({\rm PtS}_2)$$

$$\Delta\mu_{\rm Hg} + \Delta\mu_{\rm S} = \Delta H({\rm HgS})$$

Table SI Gibbs Free Energy of SACs

Defects	Gibbs Free Energy (eV)
Sc _{In}	2.06
Ti _{In}	0.61 0.50
${co}_{In}$ ${co}_{In}$	0.50 2.14
$\operatorname{Zr}_{\operatorname{In}}$	0.37
Cd _{In}	0.64
La _{In}	2.20
Ce _{In}	1.31
Pr_{In}	2.18
$\mathrm{Nd}_{\mathrm{In}}$	2.18
Pm_{In}	2.16
Sm_{In}	2.16
Eu_{In}	0.63
Gd_{In}	2.14
Tb_{In}	2.14
Dy_{In}	2.13
Ho_{In}	2.12
Er_{In}	2.12
Tm_{In}	2.11
Yb_{In}	1.06
Lu _{In}	2.10
Hf_{In}	0.32
Ta _{In}	0.30
Hg _{In}	0.91
Sc_{Zn}	0.97
Mn_{Zn}	1.04 0.49
Ni _{Zn}	0.49
Y_{Zn}	0.92
Tc _{Zn} Cd _{Zn}	2.27
La_{Zn}	0.81
Ce _{Zn}	0.85
Pr _{Zn}	0.83
Nd _{Zn}	0.86
Pm _{Zn}	0.89
Sm _{Zn}	0.90
Eu _{Zn}	2.20
$\operatorname{Gd}_{\operatorname{Zn}}$	0.92
Tb_{Zn}	3.37
$\mathrm{Dy}_{\mathrm{Zn}}$	3.37
Ho_{Zn}	3.37
$\mathrm{Er}_{\mathrm{Zn}}$	0.94
Tm_{Zn}	0.95
Yb_{Zn}	2.20
Lu_{Zn}	0.95
Hg_{Zn}	2.20
Ag_S	3.08
Au_S	0.19
Cui	0.95
Y_i	0.91
Agi	2.81
La _i	0.20
Nd _i Eu _i	6.42 0.24
Eu _i Gd _i	0.24
Gu _i Tm _i	0.93
Yb _i	0.93
Hf _i	1.12
Au _i	0.30
Hg _i	0.93
**61	0.75

1-